Article

MMS

The pull-in instability and eigenfrequency variations of a graphene resonator under electrostatic loading

Yin Zhang

State Key Laboratory of Nonlinear Mechanics (LNM), Institute of Mechanics, Chinese Academy of Sciences, Beijing, China; School of Engineering Science, University of Chinese Academy of Sciences, Beijing, China

Ya-pu Zhao[iD]

State Key Laboratory of Nonlinear Mechanics (LNM), Institute of Mechanics, Chinese Academy of Sciences, Beijing, China; School of Engineering Science, University of Chinese Academy of Sciences, Beijing, China

Abstract

A continuum membrane model is presented to describe the pull-in instability and eigenfrequency variations of a graphene resonator under an electrostatic loading. The pull-in instability leads to the device failure and the eigenfrequency variation determines its frequency tuning range, which are among the most important aspects in a micro/nanomechanical resonator design. The von Kármán kinematic assumptions are used for the membrane large deflection. The geometric nonlinearity resulting from a large deflection and the physical nonlinearity resulting from an electrostatic loading are the two competing mechanisms: the geometric nonlinearity stiffens the membrane structure and the physical nonlinearity softens it. The effects of these two competing mechanisms together with the initial tensile strain on the pull-in instability and eigenfrequency variations are vividly demonstrated. With the aim of achieving a higher accuracy, a multimodal computation method together with its convergence study and error analysis is also presented.

1. Introduction

Because of its exceptional mechanical strength [1,2] and capability to sustain large electrical current [3], graphene is an excellent material for the nanoelectromechanical systems (NEMSs) [4,5]. Graphene is also with large Young's modulus, small mass density, high thermal conductivity, material robustness and

Corresponding author:

Ya-pu Zhao, State Key Laboratory of Nonlinear Mechanics (LNM), Institute of Mechanics, Chinese Academy of Sciences, No. 15 Beisihuanxi Road, Beijing 100190, China.
Email: yzhao@imech.ac.cn

stability, and so on, which thus makes it an ideal material for a mechanical resonator [1,4]. The (high) natural frequency/eigenfrequency and quality factor are the two key parameters to evaluate the performance of a mechanical resonator [6–8]. The (first) eigenfrequency of a graphene-based mechanical resonator can be extremely high due to its excellent material properties and size effect. For example, the first eigenfrequency of a circular graphene resonator with a diameter of 500 nm easily exceeds one Giga-Hertz (GHz, 10^9 Hz) [4]. Many practical applications of the micro/nanomechanical resonators, such as mass sensing [8–10], have been demonstrated. Furthermore, micro/nanomechanical resonators are with very high eigenfrequencies due to their small dimensions, which makes them the few "macroscopic" systems capable of demonstrating the quantum effect [11], which plays a more and more important role in the fundamental research. The graphene-based mechanical resonator is an important and ideal device in the quantum-electromechanical systems (QEMSs) [4]. Because of its high mechanical strength, a graphene-based mechanical resonator can take a very large tensile stress, which enhances both the eigenfrequency and quality factor [7,8,12].

Although graphene physically is the discrete system of a single layer carbon atoms tied together by the covalent C–C bonds [3], the validity and effectiveness of the continuum elasticity modeling for graphene have been demonstrated [13–15]. The doubly clamped rectangular graphene resonator [1] usually suffers the inhomogeneous strains and ill-defined mode shapes [5], which presents significant challenges in the resonator applications [16]. Furthermore, because of the strong interactions between the edges of a rectangular graphene resonator and the supporting substrate [17], the energy dissipation is very significant, which thus results in a low quality factor [18]. A circular graphene-based resonator can be easily formed by simply depositing a graphene on a substrate with a circular hole [13,14]. The edge and corner-free circular graphene resonator can alleviate the above inhomogeneity and energy dissipation problems [19]. Here, the continuum model of a circular membrane is applied to the graphene-based resonator under a large built-in stress. Since a suspended structure and an actuating electrode form a parallel capacitor, the electrostatic force provides a convenient, efficient and fast-response actuation mechanism in many NEMS devices [20–23]. The electrostatic force is physically nonlinear as it is inversely proportional to the gap distance between the structure and electrode. Because of its softening effect, the electrostatic force finally leads to an instability called pull-in [20] at which a structure snaps to contact with the electrode. On the other side, when the maximum center displacement of a suspended plate/membrane exceeds its thickness, the linear theory becomes inaccurate and nonlinear theory must be adopted [24–26]. The nonlinear theory here is based on the von Kármán kinematic assumptions, which in essence introduce more items into strains to account for the large deflections of a structure [24–26]. The geometric nonlinearity arises from the large deflection, which stiffens a structure through the (nonlinear) effects of the mid-plane stretching and/or curvature. As the membrane deflection varies with the electrostatic loading, the physical and geometric nonlinearities also change. The competition between the physical and geometric nonlinearities results in the eigenfrequency variation, or say, the frequency tuning [14], which is very important in a resonator application.

Around the pull-in instability points at which the structure effective stiffness becomes zero, a tiny variation of loading induces an enormous change of deflection [20]. Therefore, it imposes a significant challenge of accurately computing the structure deflection and eigenfrequency around those pull-in points [27]. The membrane model incorporating the nonlinearities of both the electrostatic loading and large deflection is presented together with a multimodal computation method. The computation consists of two major parts: the computations of equilibrium and eigenfrequency. The eigenfrequencies are computed after the Taylor series expansion on the electrostatic force and the linearization around the corresponding equilibria. In this study, two different eigenfrequency variation patterns are found: the first eigenfrequency experiences the monotonic decrease and all other higher eigenfrequencies are the decrease–increase pattern as the electrostatic force increases. The aforementioned two nonlinearities are the major mechanisms responsible for the eigenfrequency variation patterns. To ensure the computational accuracy, the convergence study and truncation error analysis on the mode and the Taylor series expansion numbers are presented. There are many studies which simplify a continuum resonator as the 1-degree-of-freedom (1-DOF) model of the Duffing equation [28]. The resonator vibration described by the Duffing equation can indeed yield good results in certain scenarios [28]. However, the 1-DOF Duffing equation, which is often obtained by the one mode approximation [20], contains only the cubic nonlinearity. For this particular scenario of a membrane with large deflection and electrostatic loading,

our multimodal computation method shows that the minimum of four modes and the terms up to the sextic nonlinearity must be maintained to reach the convergence and satisfying accuracy. Our computation shows that there are many modes participating in the membrane deflection and the modal amplitudes varying with the electrostatic loading. This modal amplitude variation also means the shape change of the membrane deflection. The fixed deflection shape of a membrane at different loadings [14], which significantly simplifies the computation, can thus introduce an error more or less [25]. Besides a straightforward method for the eigenfrequency computation, our multimodal computation method also provides a systematic way of evaluating the computational accuracy.

2. Model development

For the large deflection of a circular plate/membrane, the von Kármán kinematic assumptions in the polar coordinate system of (r, θ) are the following [24,25]:

$$\epsilon_r = \frac{N_r - \nu N_t}{Eh} = \frac{\partial u}{\partial r} + \frac{1}{2}\left(\frac{\partial w}{\partial r}\right)^2 + \epsilon_o, \quad \epsilon_t = \frac{N_t - \nu N_r}{Eh} = \frac{u}{r} + \epsilon_o, \tag{1}$$

where ϵ_r and ϵ_t are the radial and circumferential strains, respectively; N_r and N_t are the radial and circumferential tensions per arc length, respectively; u and w are the in-plane and out-of-plane displacements, respectively; E and ν are Young's modulus and Poisson's ratio, respectively; ϵ_o is the initial tensile strain and $\epsilon_o = (1 - \nu)N_o/(Eh)$ (N_o is the initial tension per arc length). In the above equation, u and w are implicitly assumed axisymmetric, i.e., u and w are independent of the azimuth angle (θ). In the plate/membrane vibration, the nonaxisymmetric $\theta-$dependent modes are the degenerate ones [29]. In the degenerate modes, one eigenfrequency/resonant frequency corresponds to infinite eigenvectors/mode shapes [29], which makes their identification in the spectrum analysis extremely challenging [30] and thus enormous difficulty in the membrane resonator sensor applications [16]. In the applications of the mass resonator sensor, the quintessential problem is to solve the inverse problem of determining the adsorbate mass by the shifts of eigenfrequencies [8–10], which becomes extremely difficult if not impossible with the presence of the degenerate modes [16]. Therefore, systematic measures have been carried out to ensure no occurrence of the degenerate modes in a membrane resonator sensor [30–32]. Two effective ones are in the fabrication process: to eliminate/lessen the surface contamination [30] and peeling-off at the membrane clamped end [32]. Both measures in essence are to ensure the axisymmetry of a membrane structure. The above axisymmetric assumptions of u and w are to exclude the degenerate modes.

Figure 1(a) is the schematic diagram of a graphene deposited on a substrate with a circular hole and the related dimensions are shown in Figure 1(b). The kinetic energy of the graphene membrane is as follows [33]:

$$T = \int\limits_0^{2\pi}\int\limits_0^a \frac{m}{2}\left[\left(\frac{\partial u}{\partial t}\right)^2 + \left(\frac{\partial w}{\partial t}\right)^2\right]rdrd\theta = \pi m \int\limits_0^a\left[\left(\frac{\partial u}{\partial t}\right)^2 + \left(\frac{\partial w}{\partial t}\right)^2\right]rdr, \tag{2}$$

where a is the radius of the suspended circular graphene, and m is the mass per unit area and $m = \rho h$ (ρ is the density and h is the membrane thickness). The membrane stretching energy of V_s is given as follows [24,25]:

$$V_s = 2\pi \int\limits_0^a\left(\frac{N_r \epsilon_r}{2} + \frac{N_t \epsilon_t}{2}\right)rdr = \frac{\pi Eh}{1 - \nu^2}\int\limits_0^a\left(\epsilon_r^2 + \epsilon_t^2 + 2\nu\epsilon_r\epsilon_t\right)rdr. \tag{3}$$

The graphene sheet is with some bending stiffness and thus bending energy [2]. While the graphene sheet is often under remarkably high in-plane tension due to either the residual stress [2,12] or the intentional enhancement to improve the resonator performance [5,12]. The in-plane tension is so high and even higher than the fracture strength of most materials [2,12]. The tension inside a micro/
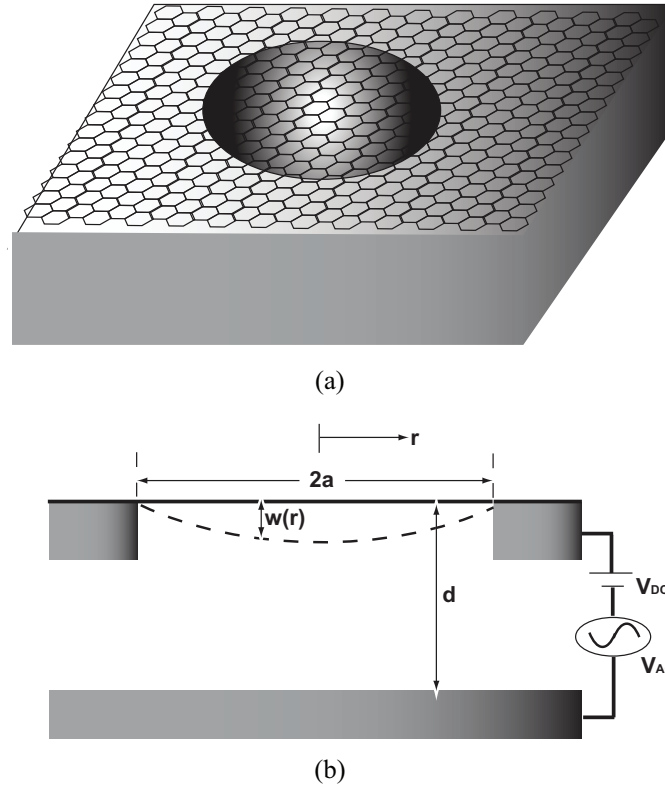
(a)

(b)

Figure 1. (a) Schematic diagram of a graphene layer deposited on a substrate with a circular hole. (b) The dimensions of the graphene and electrode.

nanomechanical resonator enhances both the eigenfrequencies and quality factor, which are the much sought-after properties in the applications of a resonator [6,7]. In this study, the initial tensile strain ϵ_o ranges from 10^{-3} to 10^{-2}. With such large in-plane tension, the stretching energy is several orders of magnitude larger than the bending energy [16]. Therefore, a graphene sheet is modeled as a membrane rather a plate by ignoring the bending energy [5,12,14].

The external work done by the electrostatic force (W_e) is the following [20]:

$$W_e = 2\pi \int_0^a qwrdr = \pi \int_0^a \frac{\epsilon V^2 w}{(d-w)^2} rdr, \tag{4}$$

where q is the (transverse) electrostatic force per unit area and $q = \epsilon V^2/2(d-w)^2$ (ϵ is the dielectric constant, V is the applied voltage, and d is the gap distance between the graphene and electrode). As seen in Figure 1(b), the applied voltage V are in two parts as follows: $V = V_{DC} + V_{AC}$. Here, V_{DC} and V_{AC} are the direct current (DC) and the alternating current (AC) voltages, respectively. In the applications of the devices driven by an electrostatic force, V_{DC} is used to (statically) deform the device structure to a certain equilibrium and V_{AC} is then to drive the device to vibrate around that equilibrium [34].

The governing equation of the graphene membrane vibration is derived by the Hamilton principle, i.e., $\delta \int_{t_1}^{t_2} (T - V_s + W_e)dt = 0$. During the derivation, the substitution of ϵ_r and ϵ_t in equation (1) into the V_s expression of equation (3) is quite lengthy and messy, which is omitted here. The governing equations are directly given as follows:

$$m\frac{\partial^2 w}{\partial t^2} - N_o\left(\frac{1}{r}\frac{\partial w}{\partial r} + \frac{\partial^2 w}{\partial r^2}\right) - \frac{Eh}{1-\nu^2}\left[\frac{1}{r}\frac{\partial u}{\partial r}\frac{\partial w}{\partial r} + \frac{\partial^2 u}{\partial r^2}\frac{\partial w}{\partial r} + \frac{\partial u}{\partial r}\frac{\partial^2 w}{\partial r^2} + \frac{\nu}{r}\left(\frac{\partial u}{\partial r}\frac{\partial w}{\partial r} + u\frac{\partial^2 w}{\partial r^2}\right)\right]$$
$$- \frac{Eh}{1-\nu^2}\left[\frac{1}{2r}\left(\frac{\partial w}{\partial r}\right)^3 + \frac{3}{2}\left(\frac{\partial w}{\partial r}\right)^2\frac{\partial^2 w}{\partial r^2}\right] - \frac{\epsilon V^2}{2(d-w)^2} = 0, \tag{5}$$

and

$$m\frac{\partial^2 u}{\partial t^2} - \frac{Eh}{1-\nu^2}\left(\frac{\partial^2 u}{\partial r^2} + \frac{1}{r}\frac{\partial u}{\partial r} - \frac{u}{r^2}\right) - \frac{Eh}{1-\nu^2}\left[\frac{1-\nu}{2r}\left(\frac{\partial w}{\partial r}\right)^2 + \frac{\partial w}{\partial r}\frac{\partial^2 w}{\partial r^2}\right] = 0. \tag{6}$$

During the derivations, the relation of $\varepsilon_o = (1 - \nu)N_o/(Eh)$ is used. Besides the coupling between w and u, there are two characteristics of the above governing equations. First, there are both the quadratic and cubic nonlinearities in equation (5). The quadratic terms are:

$$\frac{1}{r}\frac{\partial u}{\partial r}\frac{\partial w}{\partial r} + \frac{\partial^2 u}{\partial r^2}\frac{\partial w}{\partial r} + \frac{\partial u}{\partial r}\frac{\partial^2 w}{\partial r^2} + \frac{\nu}{r}\left(\frac{\partial u}{\partial r}\frac{\partial w}{\partial r} + u\frac{\partial^2 w}{\partial r^2}\right),$$

and the cubic terms are:

$$\frac{1}{2r}\left(\frac{\partial w}{\partial r}\right)^3 + \frac{3}{2}\left(\frac{\partial w}{\partial r}\right)^2\frac{\partial^2 w}{\partial r^2}.$$

In comparison, there is only quadratic nonlinearity in equation (6), which is:

$$\frac{1-\nu}{2r}\left(\frac{\partial w}{\partial r}\right)^2 + \frac{\partial w}{\partial r}\frac{\partial^2 w}{\partial r^2}.$$

Those nonlinearities are all geometric ones due to the membrane large deflection, which stiffens a structure, or say, increases its eigenfrequencies. Second, the nonlinear electrostatic force ($\epsilon V^2/2(d-w)^2$) only shows in equation (5). The effect of electrostatic force on the in-plane displacement u is indirect through the quadratic terms of w in equation (6). The nonlinearity of electrostatic force is a physical one. As a structure deflects, the gap distance $(d - w)$ between the electrode and structure shrinks. Therefore, the electrostatic force increases and then eventually leads to an instability called pull-in Dorfmann and Ogden [35]. At a critical pull-in point, the graphene will suddenly collide with the electrode, which is similar to the scenario of the bifurcation of the spherical shape of a dieletric balloon under electric actuation into a pear shape [36]. The competition between the geometric and physical nonlinearities causes some interesting variation patterns of the membrane eigenfrequencies as shown later in details. The above two membrane governing equations in essence are the von Kármán plate model without the bending stiffness [25]. As discussed above, the plate/membrane geometric nonlinearity arises from the large deflection, which is dependent on the magnitude of externally applied load. This nonlinearity dependence on the external loads rather than the plate/membrane intrinsic properties, such as plate dimensions and material properties, leads to a problem called as "a hierarchy of two-dimensional models" [37]. This hierarchy problem is overcome by the *uniformly valid asymptotic plate theory* developed by Dai and his collaborators [38,39]. The expression of "uniformly valid" means that the asymptotic plate theory is independent on the external loads [38,39]. Furthermore, an (implicit) assumption in the von Kármán plate model is the linear elasticity as indicated by equation (1). A more general model called the *consistent finite-strain plate theory* based on the nonlinear elasticity and three-dimensional modeling was developed by Dai and Song [40].

The Hamilton principle also gives the following four boundary conditions:

$$\frac{\partial w}{\partial r}(0) = 0, \quad w(a) = 0, \quad u(0) = 0, \quad u(a) = 0. \tag{7}$$

The following quantities are introduced to nondimensionalize the governing equations:

$$\xi = \frac{r}{a}, \quad W = \frac{w}{d}, \quad U = \frac{u}{d}, \quad \tau = \sqrt{\frac{Eh^2}{(1-\nu^2)ma^3}}t. \tag{8}$$

Now equations (5) and (6) are nondimensionalized as the following:

$$\frac{\partial^2 W}{\partial \tau^2} - \alpha_1 \left(\frac{1}{\xi} \frac{\partial W}{\partial \xi} + \frac{\partial^2 W}{\partial \xi^2} \right) - \alpha_2 \left[\frac{1}{\xi} \frac{\partial U}{\partial \xi} \frac{\partial W}{\partial \xi} + \frac{\partial^2 U}{\partial \xi^2} \frac{\partial W}{\partial \xi} + \frac{\partial U}{\partial \xi} \frac{\partial^2 W}{\partial \xi^2} + \frac{\nu}{\xi} \left(\frac{\partial U}{\partial \xi} \frac{\partial W}{\partial \xi} + U \frac{\partial^2 W}{\partial \xi^2} \right) \right]$$
$$- \alpha_3 \left[\frac{1}{2\xi} \left(\frac{\partial W}{\partial \xi} \right)^3 + \frac{3}{2} \left(\frac{\partial W}{\partial \xi} \right)^2 \frac{\partial^2 W}{\partial \xi^2} \right] - \frac{\alpha_4}{(1-W)^2} = 0, \tag{9}$$

$$\frac{\partial^2 U}{\partial \tau^2} - \alpha_5 \left(\frac{\partial^2 U}{\partial \xi^2} + \frac{1}{\xi} \frac{\partial U}{\partial \xi} - \frac{U}{\xi^2} \right) - \alpha_2 \left[\frac{1-\nu}{2\xi} \left(\frac{\partial W}{\partial \xi} \right)^2 + \frac{\partial W}{\partial \xi} \frac{\partial^2 W}{\partial \xi^2} \right] = 0. \tag{10}$$

Here, the dimensionless parameters of α_is ($i = 1$–5) are defined as follows:

$$\alpha_1 = \frac{(1-\nu^2)aN_o}{Eh^2} = \frac{(1+\nu)a\epsilon_o}{h}, \quad \alpha_2 = \frac{d}{h}, \quad \alpha_3 = \frac{d^2}{ah}, \quad \alpha_4 = \frac{\epsilon V^2 (1-\nu^2)a^3}{2Ed^3h^2}, \quad \alpha_5 = \frac{a}{h}. \tag{11}$$

here α_1 indicates the (dimensionless) initial strain/stress; α_4 is the (dimensionless) electrostatic loading; α_2, α_3, and α_5 characterize the membrane geometry. To compute the eigenfrequencies of the membrane, we divide W and U separately into two parts as the following:

$$U(\tau, \xi) = U_o(\xi) + U_1(\tau, \xi), \quad W(\tau, \xi) = W_o(\xi) + W_1(\tau, \xi), \tag{12}$$

where $U_o(\xi)$ and $W_o(\xi)$ are the equilibria (under different DC electrostatic loadings); $U_1(\tau, \xi)$ and $W_1(\tau, \xi)$ are the small oscillations around the equilibria due to the AC loading. The following governing equations for $U_o(\xi)$ and $W_o(\xi)$ are derived from equations (9) and (10) by eliminating the time-related terms:

$$\alpha_1 \left(\frac{1}{\xi} \frac{\partial W_o}{\partial \xi} + \frac{\partial^2 W_o}{\partial \xi^2} \right) + \alpha_2 \left[\frac{1}{\xi} \frac{\partial U_o}{\partial \xi} \frac{\partial W_o}{\partial \xi} + \frac{\partial^2 U_o}{\partial \xi^2} \frac{\partial W_o}{\partial \xi} + \frac{\partial U_o}{\partial \xi} \frac{\partial^2 W_o}{\partial \xi^2} + \frac{\nu}{\xi} \left(\frac{\partial U_o}{\partial \xi} \frac{\partial W_o}{\partial \xi} + U_o \frac{\partial^2 W_o}{\partial \xi^2} \right) \right]$$
$$+ \alpha_3 \left[\frac{1}{2\xi} \left(\frac{\partial W_o}{\partial \xi} \right)^3 + \frac{3}{2} \left(\frac{\partial W_o}{\partial \xi} \right)^2 \frac{\partial^2 W_o}{\partial \xi^2} \right] + \frac{\alpha_4}{(1-W_o)^2} = 0, \tag{13}$$

$$\alpha_5 \left(\frac{\partial^2 U_o}{\partial \xi^2} + \frac{1}{\xi} \frac{\partial U_o}{\partial \xi} - \frac{U_o}{\xi^2} \right) + \alpha_2 \left[\frac{1-\nu}{2\xi} \left(\frac{\partial W_o}{\partial \xi} \right)^2 + \frac{\partial W_o}{\partial \xi} \frac{\partial^2 W_o}{\partial \xi^2} \right] = 0. \tag{14}$$

The eigenfrequency is the concept for a linear system; we need to linearize equations (9) and (10). First, the electrostatic force in equation (9) is linearized via the Taylor series expansion as the following:

$$\frac{\alpha_4}{(1-W)^2} = \frac{\alpha_4}{1 - 2W + W^2} \approx \alpha_4 \left[1 + \sum_{k=1}^{M} (k+1)W^k \right] \approx \alpha_4 \left[1 + \sum_{k=1}^{M} (k+1)W_o^k \right]$$
$$+ \alpha_4 \left[1 + \sum_{k=1}^{M} (k+1)kW_o^{k-1} \right] W_1, \tag{15}$$

where M is the number of the Taylor series expansions. In conjunction with equations (12)–(15), the linearizations of equations (9) and (10) around the equilibria of U_o and W_o are carried out. After some rearrangements, equation (9) is now linearized as the following:

$$\frac{\partial^2 W_1}{\partial \tau^2} - \alpha_1 \left(\frac{1}{\xi} \frac{\partial W_1}{\partial \xi} + \frac{\partial^2 W_1}{\partial \xi^2} \right) - \alpha_2 \left[\frac{(1+\nu)}{\xi} \frac{\partial U_o}{\partial \xi} \frac{\partial W_1}{\partial \xi} + \frac{(1+\nu)}{\xi} \frac{\partial W_o}{\partial \xi} \frac{\partial U_1}{\partial \xi} + \frac{\partial^2 U_o}{\partial \xi^2} \frac{\partial W_1}{\partial \xi} + \frac{\partial W_o}{\partial \xi} \frac{\partial^2 U_1}{\partial \xi^2} \right.$$

$$+ \frac{\partial U_o}{\partial \xi} \frac{\partial^2 W_1}{\partial \xi^2} + \frac{\partial^2 W_o}{\partial \xi^2} \frac{\partial U_1}{\partial \xi} + \frac{\nu}{\xi} \left(U_o \frac{\partial^2 W_1}{\partial \xi^2} + \frac{\partial^2 W_o}{\partial \xi^2} U_1 \right) \Bigg]$$

$$- \alpha_3 \left[\frac{3}{2\xi} \left(\frac{\partial W_o}{\partial \xi} \right)^2 \frac{\partial W_1}{\partial \xi} + 3 \frac{\partial W_o}{\partial \xi} \frac{\partial^2 W_o}{\partial \xi^2} \frac{\partial W_1}{\partial \xi} + \frac{3}{2} \left(\frac{\partial W_o}{\partial \xi} \right)^2 \frac{\partial^2 W_1}{\partial \xi^2} \right] - \alpha_4 \left[1 + \sum_{k=1}^{M} (k+1)k W_o^{k-1} \right] W_1 = 0.$$

$$(16)$$

Similarly, equation (10) is now linearized to become the following:

$$\frac{\partial^2 U_1}{\partial \tau^2} - \alpha_5 \left(\frac{\partial^2 U_1}{\partial \xi^2} + \frac{1}{\xi} \frac{\partial U_1}{\partial \xi} - \frac{U_1}{\xi^2} \right) - \alpha_2 \left[\frac{(1-\nu)}{\xi} \frac{\partial W_o}{\partial \xi} \frac{\partial W_1}{\partial \xi} + \frac{\partial W_o}{\partial \xi} \frac{\partial^2 W_1}{\partial \xi^2} + \frac{\partial^2 W_o}{\partial \xi^2} \frac{\partial W_1}{\partial \xi} \right] = 0. \qquad (17)$$

Due to the coupling between the in-plane and out-of-plane displacements, solving equations (13) and (14) is "notoriously difficult" [41], which presents a two-point boundary value problem [25]. Furthermore, the eigenvalue problems of equations (16) and (17) also become very complex and difficult because of the coupling. Here, we de-couple the governing equations to simplify the problem. For sure, the de-coupling sacrifices some accuracy. While, as shown in Appendix 1, the first eigenfrequency of the in-plane displacement (U_1) is even larger than the tenth of the out-of-plane displacement (W_1). This huge eigenfrequency difference can also be inferred from equation (17): the linear stiffness terms are associated with α_5, which is defined in equation (11) and is a very large number especially for a graphene structure. Dynamically, when the lower out-of-plane modes are excited, which is also the application scenario of a graphene resonator [14], there is almost no in-plane displacement excited because of this huge eigenfrequency difference. This huge eigenfrequency difference leads to a rather weak coupling, or say, the in-plane displacements can be treated "adiabatically" [14], which is the physical mechanism to de-couple the governing equation without too much accuracy to be sacrificed [33].

For the governing equation of the out-of-plane displacement (W_1), the decoupled equilibrium equation of equation (13) is as follows:

$$\alpha_1 \left(\frac{1}{\xi} \frac{\partial W_o}{\partial \xi} + \frac{\partial^2 W_o}{\partial \xi^2} \right) + \alpha_3 \left[\frac{1}{2\xi} \left(\frac{\partial W_o}{\partial \xi} \right)^3 + \frac{3}{2} \left(\frac{\partial W_o}{\partial \xi} \right)^2 \frac{\partial^2 W_o}{\partial \xi^2} \right] + \frac{\alpha_4}{(1-W_o)^2} = 0. \qquad (18)$$

The linearized equation of motion of equation (16) now becomes the following:

$$\frac{\partial^2 W_1}{\partial \tau^2} - \alpha_1 \left(\frac{1}{\xi} \frac{\partial W_1}{\partial \xi} + \frac{\partial^2 W_1}{\partial \xi^2} \right) - \alpha_3 \left[\frac{3}{2\xi} \left(\frac{\partial W_o}{\partial \xi} \right)^2 \frac{\partial W_1}{\partial \xi} + 3 \frac{\partial W_o}{\partial \xi} \frac{\partial^2 W_o}{\partial \xi^2} \frac{\partial W_1}{\partial \xi} + \frac{3}{2} \left(\frac{\partial W_o}{\partial \xi} \right)^2 \frac{\partial^2 W_1}{\partial \xi^2} \right]$$

$$- \alpha_4 \left[1 + \sum_{k=1}^{M} (k+1)k W_o^{k-1} \right] W_1 = 0.$$

$$(19)$$

The membrane equilibrium of W_o as given in equation (18) needs to be obtained first. With the substitution of the W_o solution into equation (19), the eigenfrequencies can then be found. Here, the Galerkin method is used for the numerical computation, which assumes the following expression for W_o and W_1:

$$W_o(\xi) = \sum_{j=1}^{N} A_j J_o\left(\eta_j \xi \right), \quad W_1(\xi, \tau) = \sum_{j=1}^{N} a_j(\tau) J_o\left(\eta_j \xi \right), \qquad (20)$$

where J_o is the first kind of the Bessel function of order 0 [42]; η_js are the zero points of J_o and their values are given in Appendix 1. Here, $J_o(\eta_j \xi)$ is the axisymmetric mode of a circular membrane [29], which is independent of the azimuth angle. A_js are the constants, which is the static modal amplitude to be

determined for different electrostatic loadings of α_4; $a_j(\tau)$ is the dynamic modal amplitudes; N is the mode number. By timing $\xi J_o(\eta_i \xi)$ and integrating from 0 to 1, equation (18) becomes the following:

$$\alpha_1 \int_0^1 \xi J_o(\eta_i \xi) \left(\frac{1}{\xi} \frac{\partial W_o}{\partial \xi} + \frac{\partial^2 W_o}{\partial \xi^2} \right) d\xi + \alpha_3 \int_0^1 \xi J_o(\eta_i \xi) \left[\frac{1}{2\xi} \left(\frac{\partial W_o}{\partial \xi} \right)^3 + \frac{3}{2} \left(\frac{\partial W_o}{\partial \xi} \right)^2 \frac{\partial^2 W_o}{\partial \xi^2} \right]$$

$$d\xi + \alpha_4 \int_0^1 \frac{\xi J_o(\eta_i \xi)}{(1 - W_o)^2} d\xi = 0. \tag{21}$$

By the substitution of W_o into equation (20) and application of the orthogonality property of J_o[29], equation (21) becomes a nonlinear algebraic equation set of A_js, which is solved by the Newton–Raphson method [43]. It is noticed that in equation (18) or equation (21), there is neither any linearization process nor the Taylor series expansion involved. To expand the nonlinear electrostatic force term into the Taylor series is a "quick and dirty" solution as commented by Gutschmidt [27], which may cause the poor accuracy even large number of modes used in the computation. The nonlinear form of equation (18) or equation (21) is to ensure the computation accuracy of the equilibrium. In contrast, eigenfrequency is the concept in a linear system, the linearization and the Taylor series expansion must be used to obtain the linear equation of equation (19).

Once the equilibrium W_o is solved via equation (21), or say, the values of A_js are obtained, we substitute the W_o solution into equation (19) and apply the Galerkin method again, which gives the following equation:

$$\mathbf{M}\ddot{\vec{a}} + \mathbf{K}\vec{a} = 0, \tag{22}$$

where $\vec{a} = (a_1, a_2, \ldots, a_N)^T$ is the modal amplitude vector of W_1; M is the mass matrix, which is diagonal due to the orthogonality property of the Bessel function [29]. The elements of M are with the following expressions:

$$M_{ij} = \begin{cases} \int_0^1 \xi J_o^2(\eta_i \xi) d\xi, & i = j \\ 0, & i \neq j, \end{cases} \tag{23}$$

The expression for stiffness $\mathbf{K}$ is rather complex, which is broken into three parts as $\mathbf{K} = \mathbf{K}^I + \mathbf{K}^{II} + \mathbf{K}^{III}$. Here, $\mathbf{K}^I$ is the linear stiffness terms associated with α_1, which is also diagonal due to the orthogonality property as given as follows:

$$K_{ij}^I = -\alpha_1 \int_0^1 \xi J_o(\eta_i \xi) \left[\frac{1}{\xi} \frac{dJ_o(\eta_j \xi)}{d\xi} + \frac{d^2 J_o(\eta_j \xi)}{d\xi^2} \right] d\xi = \begin{cases} \alpha_1 \eta_i^2 \int_0^1 \xi J_o^2(\eta_i \xi) d\xi, & i = j \\ 0, & i \neq j. \end{cases} \tag{24}$$

Compared with the mass matrix, $K_{ij}^I = \alpha_1 \eta_i^2 M_{ij}$. During the derivation, the following Bessel function properties are used [42]:

$$\frac{dJ_o(\eta_j \xi)}{d\xi} = -\eta_j J_1(\eta_j \xi), \quad \xi \frac{d^2 J_o(\eta_j \xi)}{d\xi^2} = \eta_j J_1(\eta_j \xi) - \eta_j^2 J_o(\eta_j \xi). \tag{25}$$

where J_1 is the first kind of the Bessel function of order 1 [42]. K^{II} is the nonlinear stiffness terms associated with α_3. In conjunction with equations (19) and (23), K^{II} is given as follows:

$$K_{ij}^{II} = \alpha_3 \eta_j \int_0^1 J_o(\eta_i\xi)J_1\left(\eta_j\xi\right)\left[\frac{3}{2}\left(\frac{dW_o}{d\xi}\right)^2 + 3\xi\frac{dW_o}{d\xi}\frac{d^2W_o}{d\xi^2}\right]d\xi + \frac{3\alpha_3\eta_j}{2}\int_0^1 J_o(\eta_i\xi)$$

$$\left[\eta_j\xi J_o\left(\eta_j\xi\right) - J_1\left(\eta_j\xi\right)\right]d\xi. \tag{26}$$

Mathematically, K^{II} is positive and nondiagonal due to the coupling effect. Physically, K^{II} is due to the membrane large deformation, which is the geometric nonlinearity and stiffens a structure.

Here, $\mathbf{K}^{III}$ is the physical nonlinear terms associated with α_4 of electrostatic force and its elements are with the following expression:

$$K_{ij}^{III} = -\alpha_4\int_0^1 \xi J_o(\eta_i\xi)J_o\left(\eta_j\xi\right)\left[1 + \sum_{k=1}^M (k+1)kW_o^{k-1}\right]d\xi. \tag{27}$$

In comparison with the positive K^{II}, K^{III} is negative and nondiagonal. Physically, K^{III} is associated with the electrostatic loading, which softens a structure by reducing its stiffness [20]. As defined in equation (11), $\alpha_4 \propto (V_{DC} + V_{AC})^2$, α_4 in general is a time-varying parameter because of V_{AC}. Therefore, the stiffness changes with time and the system vibration is a parametric one [44]. While, the linearizations of the electrostatic force and the governing equations of equations (9) and (10) around the equilibria are based on that $|V_{DC}| \ll |V_{AC}|$, which also means $|W_1| \ll |W_o|$. Therefore, equation (22) is a linear vibration with the constant stiffness. When V_{AC} is relatively large as compared with V_{DC}, instead of linearization, the parametric vibration [44] or the direct numerical computation approach [45] must be adopted.

3. Results and discussion

For the graphene membrane in this study, the following parameters are taken: radius $a = 2.5 \times 10^{-6}$ m, thickness $h = 3.4 \times 10^{-10}$ m, Poisson's ratio $\nu = 0.165$, the gap distance between the membrane and electrode $d = 2 \times 10^{-7}$ m. The above parameters are the typical ones used in the scenario of a graphene layer deposited on a substrate [15]. With these parameters and according to equation (11), the following three dimensionless parameters in this study are fixed as: $\alpha_2 = 588.2853$, $\alpha_3 = 47.0588$, and $\alpha_5 = 7352.9412$.

Before examining the results, we would like to address the bending stiffness/energy issue. As mentioned above, the graphene sheet is modeled as a membrane by ignoring its bending stiffness/energy. Due to its small thickness, the graphene bending stiffness is extremely small, e.g., the bending stiffness of a monolayer graphene varies in the range of $1\sim20$ eV (or $1.6 \times 10^{-19}\sim3.2 \times 10^{-18}$ N m) [46,47]. Besides the bending stiffness, the Gaussian stiffness, which measures the (structural) resistance to form a non-null Gaussian curvature and is with the same magnitude of the bending stiffness [46], also plays a crucial role in determining the graphene bending. The bending or say, the rippling of a graphene is the very reason for its existence as a two-dimensional material. However, the bending of a graphene changes the system initial configuration and thus the overall stiffness [15], which may vary differently for different devices and fabrication processes. Therefore, it requires the calibration/measurement for each device and this imposes significant challenges in a practical application. As mentioned before, exerting the in-plane tension is an effective method of overcoming the above issue [5,12], whose benefits are two-fold: one is to increase the eigenfrequencies of a graphene, which can improve both the resonator sensitivity and resolution [7]; the other is to flatten the graphene, which makes the impact of initial configuration much less. With the increase in the in-plane tension, the bending contribution to both the system energy and deflection becomes less and less. The key question here is: how large the in-plane tension should be when we can ignore the bending and thus model the graphene sheet as a membrane? Sheplak and Dugundji [48] defined a dimensionless parameter to address this issue for a circular plate, which is given as follows: $k = \sqrt{N_o a^2/D} = \sqrt{12(1+\nu)\epsilon_o}(a/h)$. Here, N_o, ϵ_o, and ν as defined in equation (1) are the initial tension per arc length, initial tensile strain, and Poisson's ratio, respectively. $D = Eh^3/12(1-\nu^2)$ is the plate bending stiffness (E is Young's modulus). This dimensionless number k demarcates the structure deformation behavior as follows [48]: the plate behavior dominates for $k < 1$; the membrane behavior dominates for $k > 20$ and $1 < k < 20$ is the transition zone. For a given plate structure, a, h, and ν are fixed; only ϵ_o can vary by exerting tension. To reach $k = 20$, the corresponding strain is $\epsilon_o = 5.292 \times 10^{-7}$ with

the above graphene parameters of $a = 2.5 \times 10^{-6}$ m, $h = 3.4 \times 10^{-10}$ m, and $\nu = 0.165$. This tensile strain of $\epsilon_o = 5.292 \times 10^{-7}$ is rather small, which physically means that a very small tension here can transform the graphene deformation behavior from a plate to a membrane. The mathematical reason is that the ratio of a/h is huge. In our computation, two strain values of $\epsilon_o = 5 \times 10^{-3}$ and $\epsilon_o = 1 \times 10^{-2}$ are used, which correspond to $k = 1944$ and $k = 2749$, respectively. These huge k values ensure the dominance of the membrane behavior and negligible contribution of bending.

Figure 2 examines the convergence of $W_o(0)$ on the mode number N. Here, $W_o(0)$ is the membrane center displacement, which is also the maximum one. The initial strain is set as $\epsilon_o = 5 \times 10^{-3}$, which corresponds to $\alpha_1 = 42.8309$. The membrane equation of equilibrium is equation (21) and the membrane displacement of $W(\xi)$ is expanded by the mode shapes as given in equation (20). In general, more mode shapes can more accurately describe the membrane deflection with the price of (much) more computation. In Figure 2, the mode number N is taken as $N = 1$–5. The (dimensionless) electrostatic force α_4 is increased to the critical point of the pull-in instability. The pull-in instability is the saddle-node type of instability, at which the structure effective stiffness becomes zero and the structure suddenly collapses to collide with an electrode [20], which usually leads to the device failure. Here, the physical picture of the pull-in instability can be described as follows: larger voltage means both larger electrostatic force and deflection, which leads to a larger elastic restoring force. Within the certain loading range, an equilibrium is reached because of the balance of the electrostatic and elastic restoring forces; however, the electrostatic force increases more rapidly with the increase in voltage and the pull-in instability is the critical point at which the elastic restoring force can no longer balance the electrostatic one. With the increase in voltage, the pull-in instability is ensured to occur and the collision between a structure and an electrode follows subsequently [20]. One outstanding characteristics of Figure 2 is that around the pull-in point, the displacements computed by different mode numbers all fluctuate. The inset provides a closer look at the fluctuations. Physically, the increase of the electrostatic load decreases the effective stiffness of the system, which becomes zero at the pull-in point [20]. Mathematically, this causes the Jacobian matrix used in the Newton–Raphson method to be ill-conditioned [43], which is responsible for the fluctuations. There is a way of lessening the numerical fluctuation by selecting only the odd symmetric modes in the computation [20]. In most practical applications, the applied voltage should be (far) below the pull-in one, and furthermore, the applied voltage is a control parameter. In contrast to the displacement fluctuation, there is little change of the critical pull-in voltage (α_4) and the control parameter is thus accurately computed. The α_4 value monotonically decreases from 41.625 to 40.975 as N changes from 1 to 5. The plots of $N = 4$ and $N = 5$ (almost) overlap except a tiny area around the pull-in point. The conclusion drawn from Figure 2 is that $N \geqslant 4$ is the least mode number required to ensure the computation convergence and the mechanism are explained in Figure 3.

In Figure 3, the modal amplitudes of A_js as the functions of the electrostatic force α_4 are presented. Here, to further illustrate the convergence mechanism, six modes of $N = 6$ is used. Clearly, $|A_1| > |A_2| > |A_3| > |A_4| > |A_5| > |A_6|$ is seen in Figure 3, which is also the mechanism that ensures the convergence as shown in Figure 2. The dominance of A_1 is also obvious and the inset provides a closer examinations on other modal amplitudes. The amplitudes of and A_3 and are one order and two orders of magnitudes smaller than that of A_1. In comparison, the amplitudes of A_4, A_5, and A_6 are three orders of magnitudes smaller, and moreover, A_5 and A_6 (almost) overlap. In other words, when $N = 4$ further increasing mode can only lead to very little modification of the membrane deflection, which is the very mechanism to mathematically ensure the convergence. All our following computations are with $N = 6$. In Figure 3, the variations of the modal amplitudes as the functions of electrostatic load α_4 indicate that the membrane deflection shape changes under different load. One major mechanism causing the (large) error in the computation of the plate/membrane large deflections results from the deviation of the assumed deflection shape from a real one [25]. For example, the membrane deflection shape is often assumed as $W_o(\xi) = W_o(0)(1 - \xi^2)$ [14,25], which can only capture the real deflection accurately in certain loading range. Furthermore, this assumed shape of $W_o(\xi) = W_o(0)(1 - \xi^2)$ is more suitable for the membrane deflection under a uniform pressure load not for a nonuniform electrostatic load [25]. The participation of the higher order modes in the membrane deflection reflects this nonuniform property. Because the axisymmetry of the circular membrane is assumed in equation (20), the membrane deflection is still axisymmetric with the participation of the higher order modes. The axisymmetry of a circular graphene membrane can be broken by the grain boundaries [14], and furthermore, it is not unusual
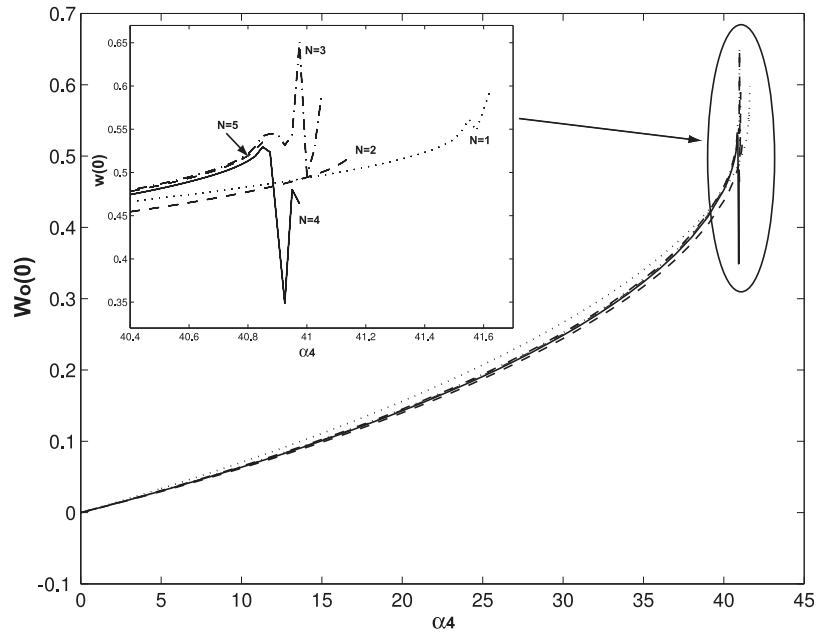
Figure 2. The convergence study of the pull-in instability on the mode number (N). Here, the initial strain $\varepsilon_o = 5 \times 10^{-3}$; $W_o(0)$ is the membrane center displacement and α_4 is the dimensionless voltage. The inset is a closer look at the membrane center deflection around the critical pull-in point.
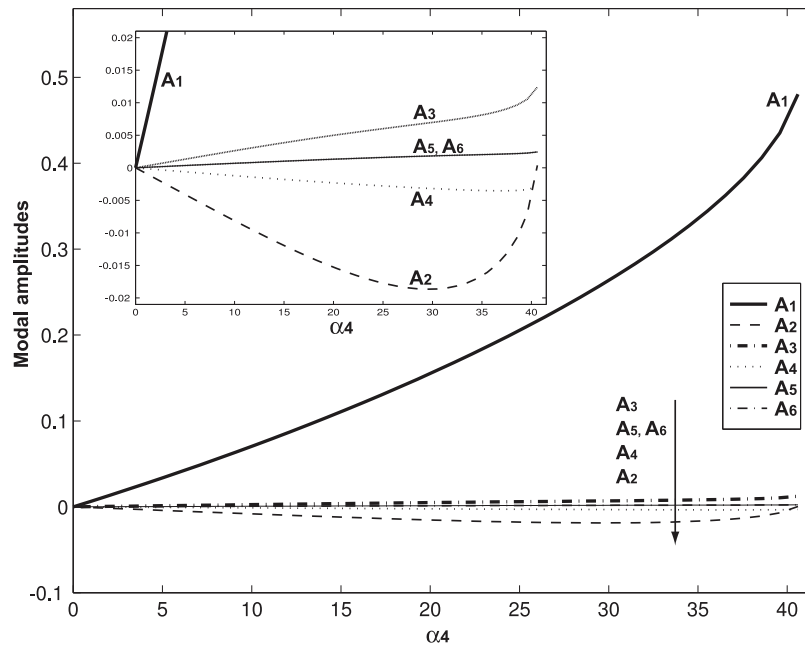

Figure 3. Modal amplitudes as the function of α_4 with the initial strain of $\varepsilon_o = 5 \times 10^{-3}$ and mode number of $N = 6$.

for a nonlinear system that an asymmetric deflection occurs in a symmetric structure under a symmetric load. The (axi)symmetry-breaking deflection can further distort the deflection shape, which makes the assumed shape less accurate.

Figure 4 shows the five plots of the membrane deflections with the different initial stretching strains ranging from $\epsilon_o = 10^{-3}$ to 10^{-2}. In Figure 4, the membrane deflections are plotted as the functions of α_4
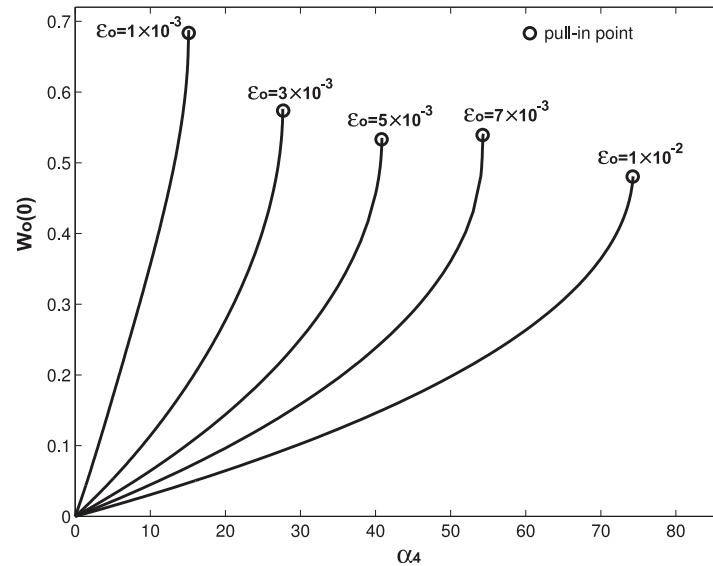
Figure 4. The pull-in instabilities of the membrane with difference initial strains (ε_os). The circles indicate the critical pull-in points.

and the pull-in instabilities are marked as the circles. One trend is clearly seen: larger initial strain ϵ_o corresponds to a larger pull-in voltage of α_4. The pull-in voltages of α_4 are 15.125, 27.65, 40.975, 54.4, and 74.3 for $\epsilon_o = 10^{-3}$, 3×10^{-3}, 5×10^{-3}, 7×10^{-3}, and 10^{-2}, respectively. Physically, the stiffness of a membrane results from its initial tension/strain. Therefore, with a larger ϵ_o, the membrane stiffness is larger and thus withholds a larger pull-in voltage, which in essence provides a larger tuning range. The other trend observed is that the slopes of the membrane deflection becomes larger with the increase in α_4, which physically indicates the decrease of the membrane effective stiffness. At the pull-in points, the slopes approach infinity and such an infinite slope is the hallmark of the structure effective stiffness becoming zero [20]. It is emphasized here that the pull-in points are the static ones, which give the upper limits [44]. In a real application, even when the electrical voltage is increased very slowly, there is still the initial effect which makes the pull-in to occur at a lower electrostatic loading of α_4 [21].

Once $W_o(\xi)$ is solved from equation (21) and substituted into equation (22), the eigenfrequencies are obtained. In equation (21), the electrostatic force keeps the nonlinear form of $\alpha_4/(1 - W_o)^2$ in order to achieve a higher accuracy in the equilibrium computation. While, the electrostatic force has to be linearized in equation (22) to obtain the eigenfrequency and this linearization process is given in equation (15). The accuracy of equation (15) depends on the expansion number M of the Taylor series. The convergence study of the membrane first eigenfrequency (ω_1) on the expansion number (M) ranging from $M = 3$ to 7 is presented in Figure 5. Here, the membrane is with the same initial strain of $\epsilon_o = 5 \times 10^{-3}$ as those in Figures 2 and 3. The computation differences are mainly around the pull-in point, i.e., α_4 around 40. The reason is that the value of W_o is large around the pull-in point and larger M, or say, more expansion terms are required to guarantee the accuracy of the Taylor series. Actually, $M = 3$ is the case that the Taylor series is only expanded to the cubic term, which is often used to (qualitatively) demonstrate the mechanism of the pull-in instability [20]. Clearly, due to the large deflection of W_o here, the $M = 3$ expansion is not accurate enough when $\alpha_4 > 35$. It is observed that in Figure 5, a larger M leads to a smaller ω_1. As mentioned above, the electrostatic force softens a structure and a larger M means the less truncation error of the electrostatic force, which enhances the softening effect and thus smaller eigenfrequencies. In contrast to the monotonically increasing slope of the membrane deflection in Figures 2 and 4, ω_1 here decreases monotonically with the increase in α_4, which is another way of indicating the reduction of the structural effective stiffness. Similarly, ω_1 approaching zero at the pull-in point indicates the zero effective stiffness, which is also often used in structural mechanics to tell the occurrence of an instability. As also seen in Figure 5, the plots of $M = 6$ and 7 overlap and a convergence is reached, or say, the effect of the higher order terms is ignorable when $M \geqslant 6$. From now on, all our eigenfrequency computations are based on $M = 7$ and $N = 6$.
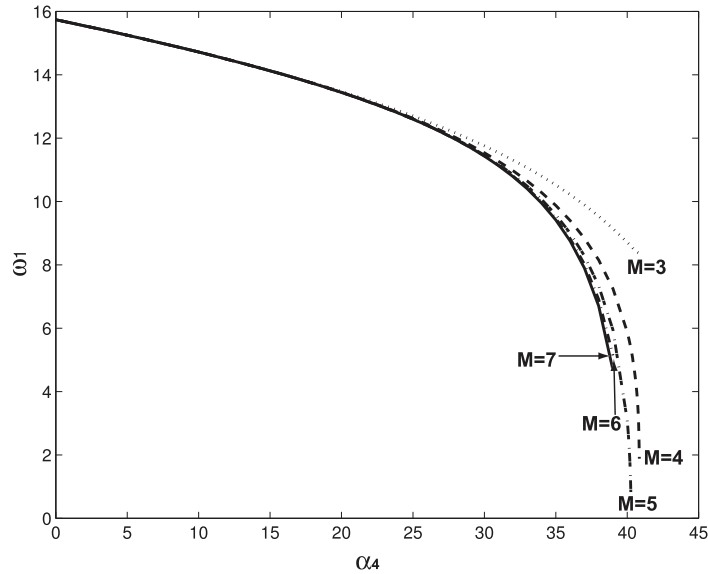
Figure 5. The convergence study of the first resonant frequency (ω_1) on the expansion number of the Taylor series (M). Here, the mode number is six ($N = 6$).
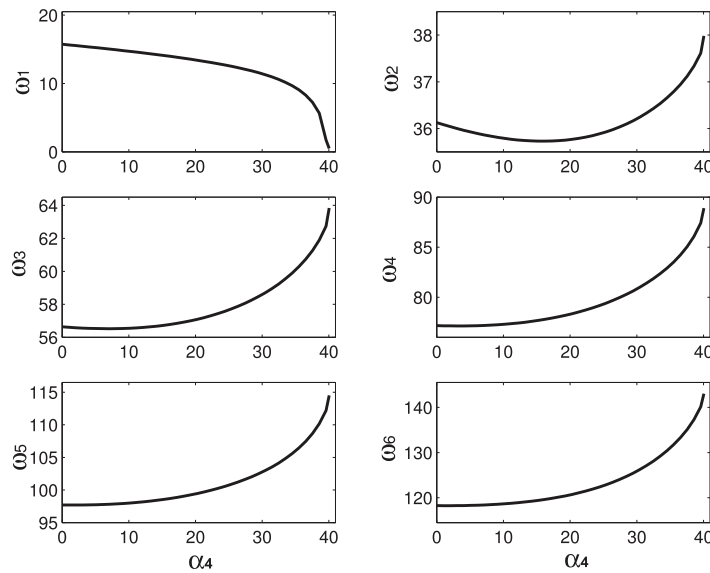

Figure 6. The first six eigenfrequencies as the functions of α_4 with $\varepsilon_o = 5 \times 10^{-3}$ and $N = M = 6$.

The first six eigenfrequencies are plotted in Figures 6 and 7 for the membrane with the two different initial strains of $\epsilon_o = 5 \times 10^{-3}$ and $\epsilon_o = 10^{-2}$, respectively. These two different initial strain scenarios share the same pattern on the eigenfrequency variation: the first eigenfrequency (ω_1) decreases monotonically with the increase in α_4 and all the other higher eigenfrequencies (from ω_2 to ω_6) decrease first and then increase. Their differences are in the variation magnitudes: ω_1 with $\epsilon_o = 5 \times 10^{-3}$ decreases from $\omega_1 = 15.738$ to zero as α_4 increases from 0 to the pull-in point of 40.975; ω_1 with $\epsilon_o = 10^{-2}$ decreases from $\omega_1 = 22.257$ to zero as α_4 increases from 0 to the pull-in point of 74.3. It is noticed that both ω_1s experience an abrupt decrease as α_4s approach their critical pull-in points. For the second eigenfrequency, ω_2 with $\epsilon_o = 5 \times 10^{-3}$ decreases first from $\omega_2 = 36.126$ at $\alpha_4 = 0$ to the minimum of $\omega_2 = 35.73$ at $\alpha_4 = 15.225$ and then increases to $\omega_2 = 37.981$ at the pull-in point of $\alpha_4 = 40.975$; in comparison, ω_2 with
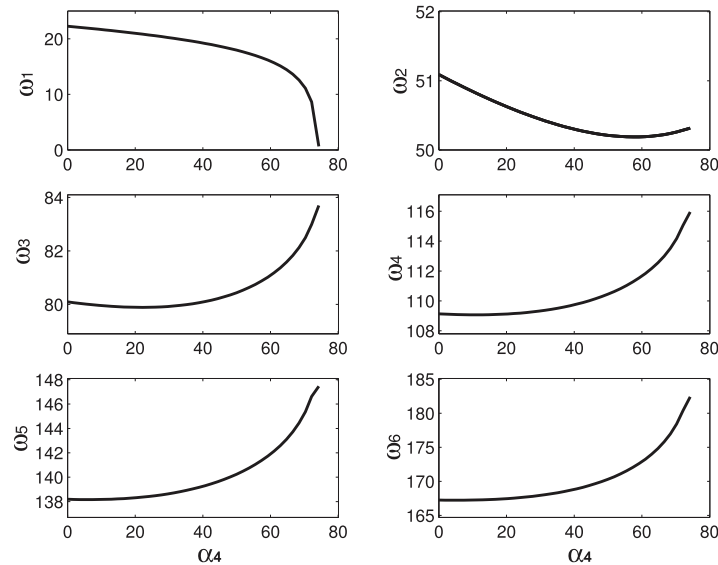
Figure 7. The first six eigenfrequencies as the functions of α_4 with $\varepsilon_o = 1 \times 10^{-2}$ and $N = M = 6$.

$\epsilon_o = 10^{-2}$ decreases first from $\omega_2 = 51.091$ at $\alpha_4 = 0$ to the minimum of $\omega_2 = 50.188$ at $\alpha_4 = 57.35$ and then increases to $\omega_2 = 50.316$ at the pull-in point of $\alpha_4 = 74.3$. For the case of $\epsilon_o = 5 \times 10^{-3}$, the second eigenfrequency is larger at the pull-in point as compared with that at the zero voltage; in comparison, the second eigenfrequency of the $\epsilon_o = 10^{-2}$ case is smaller at the pull-in point.

Here, an analysis on the pattern of the above eigenfrequency variations is presented. As mentioned above, there are two competing mechanisms on the system stiffness/eigenfrequency: the electrostatic force and large deflection. In equation (19), the electrostatic force is a physical nonlinearity. Those terms associated with α_4 are due to this physical nonlinearity, which softens the structure and thus causes the smaller eigenfrequencies and pull-in instability. As seen in Figure 1, around the pull-in point, the slopes of the deflection curves increase dramatically toward infinity. This slope increase indicates the reduction of the system (effective) stiffness. At the pull-in point, the mechanical restoring force can no longer balance the electrostatic force and the slope becomes infinity, which indicates the zero effective stiffness. As the effective stiffness decreases with the increase in the electrostatic force, ω_1 as seen in Figures 6 and 7 decreases. The large deflection is the geometric nonlinearity. Those terms associated with α_3 in equation (19) are due to this geometric nonlinearity, which gives an additional stiffness. The geometric nonlinearity of the structural large deflection can be divided into two categories: the mid-plane stretching and curvature nonlinearities. Both of these two geometric nonlinearities stiffen a structure. The competition between the physical and geometric nonlinearities leads to the monotonic decrease of ω_1 because the physical nonlinearity of the electrostatic force is a dominant one for the large initial strain case [14]. However, the geometric nonlinearity stands out in the higher modes, which leads to the increase of ω_2 to ω_6 around the pull-in points. This competition results in the monotonic decrease of the first eigenfrequency and the decrease-increase of the other higher eigenfrequencies. This competition between the physical and geometric nonlinearities is also frequently encountered in structural mechanics. Besides the competition between the two nonlinearities, the weak mode coupling also has some (indirect) contribution. When two eigenfrequencies are very close, they can either cross or diverge abruptly without a crossing (called veering). The closeness of two eigenfrequencies signals the strong mode coupling, which can lead to the mode localization and internal resonance [22,23]. The mode localization is due to the linear mode coupling [22], which is also closely related with the veering phenomenon. When a veering occurs, the two modes experience the dramatic shape changes. The internal resonance results from the nonlinear mode coupling [23], which determines the energy transfer between the modes. However, as seen in Figures 6 and 7, all the eigenfrequencies presented are well-separated, which indicates the mode coupling is very weak. This weak mode coupling is also reflected in Figure 3, in which the first modal amplitude of A_1 is always dominant. The weak mode coupling in essence reduces the modal interactions,

which lessens the system nonlinearities and makes the above two nonlinearities the dominant ones. It should be kept in mind that the mode coupling of a structure under an electrostatic loading can be significantly enhanced by its initial deflection [22,23].

Finally, we need to address the issue of the monotonic decrease of the first eigenfrequency ω_1 as presented in Figures 6 and 7. Besides the two strain scenarios of $\epsilon_o = 5 \times 10^{-3}$ and $\epsilon_o = 10^{-2}$, the ω_1s with other ϵ_os are also computed and they all show the monotonic decrease of ω_1 with the increase in the voltage α_4. Because the competition of two different nonlinearities, it is possible for the first eigenfrequency of ω_1 to increase at certain voltage range and then decrease to zero at the pull-in point in a different structural configuration. For example, the first eigenfrequency of a slacked carbon nanotube (CNT) resonator under electrostatic loading is found to increase first and then decrease to zero at the pull-in point [34]. While, this increase–decrease pattern of the first eigenfrequency is due to the CNT initial deflection, i.e., the slackness. With the presence of slackness, the CNT is modeled as an arch rather than a beam [34]. The initial deflection provides an addition geometric nonlinearity, which has significant impact on the structural dynamic properties [21–23]. The initial deflection is the major mechanism responsible for the increase–decrease pattern of the first eigenfrequency as observed by Ouakad and Younis [34]. Similarly, the frequency response of an initially curved microplate under an electrostatic loading shows the hardening behavior [49]. In comparison, the softening effects of a straight beam under an electrostatic loading are shown in its frequency response with the various combinations of the DC and AC voltages [45]. An initial deflection can induce another instability called snap-through, at which the structure flips over but without a collision with the electrode [21]. In our model, there is no such initial deflection of the graphene membrane, i.e., the membrane is taken to be flat, due to the large initial tensile strain. However, some graphenes deposited on a substrate are wrinkled [15] and wrinkling is the initial deflection. More generally, that a stress-free graphene can exist is due to the fact that it contains wrinklings [4]. Physically, the wrinkling or corrugation form of a two-dimensional structure is multifarious, which can be rather complicate and thus lead to other variation patterns of the first eigenfrequency than the monotonically decreasing one. Besides the initial strains, other parameters such as the membrane radius, thickness, and gap distance as indicated in equation (11) can also have an impact on the first eigenfrequency variation pattern of a flat membrane by introducing strong mode coupling.

4. Conclusion

A continuum membrane model is applied due to the initial large tensile strain, which simplifies the graphene resonator problem by ignoring the bending stiffness. The nonlinear governing equations are decoupled based on the huge eigenfrequency difference between the out-of-plane and in-plane displacements. The nonlinear governing equation of the out-of-plane displacement is further linearized around its equilibrium, which is reached by a (static) DC voltage. The linearization is based on that the driving AC voltage is much smaller than the DC one. For a membrane resonator with the given material, dimensions, and initial tensile strain, its linear stiffness is fixed. However, the membrane nonlinear stiffness varies with its equilibrium position, or say, deflection. The softening physical nonlinearity resulting from the electrostatic loading and stiffening geometric nonlinearity resulting from the membrane large deflection are the two competing mechanisms determining the variation patterns of the eigenfrequencies. For a two-dimensional circular membrane, the existence of degenerate modes makes the mass sensing application of a resonator extremely difficult. Besides some special measures taken in the fabrication process, the degenerate modes can also be avoided or significantly lessened by tuning the AC driving frequency away from their eigenfrequencies. Because the degenerate modes are nonaxisymmetric, the axisymmetric assumption used in this study excludes their presence. With a large electrostatic voltage, the mode coupling between the degenerate and nondegenerate modes can be enhanced, which may significantly change the dynamic properties of a resonator such as the eigenfrequency crossover, veering, mode localization and internal resonance. A more comprehensive study which includes the effects of the degenerate modes is in our future plan.

ORCID iD

Ya-pu Zhao https://orcid.org/0000-0001-9269-7404

References

[1] Bunch, JS, van der Zande, A, Verbridge, S, et al. Electromechanical resonators from graphene sheets. *Science* 2007; 314: 490–493.

[2] Lee, C, Wei, X, Kysar, JW, et al. Measurement of the elastic properties and intrinsic strength of monolayer graphene. *Science* 2008; 321: 385–388.

[3] Atalaya, J, Isacsson, A, and Kinaret, JM. Continuum elastic modeling of graphene resonators. *Nano Lett* 2008; 8: 4196–4200.

[4] Poot, M, and van der Zant, HSJ. Mechanical systems in quantum regime. *Phys Rep* 2012; 511: 273–335.

[5] Garcia-Sanchez, D, van der Zande, AM, San Paulo, A, et al. Imaging mechanical vibrations in suspended graphene sheets. *Nano Lett* 2008; 8: 1399–1403.

[6] Buks, E, and Yurke, B. Mass detection with a nonlinear nanomechanical resonator. *Phys Rev E* 2006; 74: 046619.

[7] Schmid, S, Villanueva, LG, and Roukes, ML. *Fundamentals of nanomechanical resonators*. Cham: Springer, 2016.

[8] Chaste, J, Eichler, A, Moser, J, et al. A nanomechanical mass sensor with yoctogram resolution. *Nat Nanotechnol* 2012; 7: 301–304.

[9] Naik, AK, Hanay, MS, Hiebert, WK, et al. Towards single-molecule nanomechanical mass spectrometry. *Nat Nanotechnol* 2009; 4: 445–450.

[10] Jensen, K, Kim, K, and Zettl, A. An atomic-resolution nanomechanical mass sensor. *Nat Nanotechnol* 2008; 3: 533–537.

[11] O'Connell, AD, Hofheinz, M, Ansmann, M, et al. Quantum ground state and single-phonon control if a mechanical resonator. *Nature* 2010; 464: 697–703.

[12] Kim, SY, and Park, H. On the utility of vacancies and tensile strain-induced quality factor enhancement for mass sensing using graphene monolayers. *Nanotechnology* 2010; 21: 105710.

[13] Cadelano, E, Palla, PL, Giordano, S, et al. Nonlinear elasticity of monolayer graphene. *Phys Rev Lett* 2009; 102: 235502.

[14] Eriksson, AM, Midtvedt, D, Croy, A, et al. Frequency tuning, nonlinearities and mode coupling in circular mechanical graphene resonators. *Nanotechnology* 2013; 24: 395702.

[15] Nicholl, R, Lavrik, NV, Vlassiouk, I, et al. Hidden area and mechanical nonlinearities in freestanding graphene. *Phys Rev Lett* 2017; 118: 266101.

[16] Zhang, Y, and Zhao, Y-P. Detecting the mass and position of an adsorbate on a drum resonator. *Proc R Soc A Math Phys Eng Sci* 2014; 470: 20140418.

[17] Budrikis, Z, and Zapperi, S. Temperature-dependent adhesion of graphene suspended on a trench. *Nano Lett* 2016; 16: 387–391.

[18] Kim, S, and Park, HS. The importance of edge effects on the intrinsic loss mechanisms of graphene nanoresonators. *Nano Lett* 2009; 9: 969–974.

[19] Robinson, J, Zalalutdinov, M, Baldwin, J, et al. Wafer-scale reduced graphene oxide films for nanomechanical devices. *Nano Lett* 2008; 8: 3441–3445.

[20] Zhang, Y, and Zhao, Y-P. Numerical and analytical study on the pull-in instability of micro-structure under electrostatic loading. *Sens Actuators A* 2006; 127: 366–380.

[21] Zhang, Y, Wang, Y, Li, Z, et al. Snap-through and pull-in instabilities of an arch-shaped beam under an electrostatic loading. *J Microelectromechan Syst* 2007; 16: 684–693.

[22] Hajjaj, AZ, Alfosail, F, Jaber, N, et al. Theoretical and experimental investigations of the crossover phenomenon in micromachined arch resonator: part I-linear problem. *Nonlinear Dyn* 2020; 99: 393–405.

[23] Hajjaj, AZ, Alfosail, F, Jaber, N, et al. Theoretical and experimental investigations of the crossover phenomenon in micromachined arch resonator: part II-simultaneous 1:1 and 2:1 internal resonances. *Nonlinear Dyn* 2020; 99: 407–432.

[24] Timoshenko, SP, and Woinowsky-Krieger, S. *Theory of plates and shells*. 2nd ed. New York: McGraw-Hill, 1959.

[25] Zhang, Y. Large deflection of clamped circular plate and accuracy of its approximate analytical solutions. *Sci China: Phys Mech Astron* 2016; 59: 624602.

[26] Plaut, RH. Generalized Reissner analysis of large axisymmetric deflections of thin circular and annular plates. *Int J Solids Struct* 2020; 203: 131–137.

[27] Gutschmidt, S. The influence of higher-order mode shapes for reduced-order models of electrostatically actuated microbeams. *J Appl Mech* 2010; 77: 041007.

[28] Antonio, D, Zanette, D, and López, D. Frequency stabilization in nonlinear micromechanical oscillators. *Nat Commun* 2012; 3: 806.

[29] Meirovitch, L. *Analytical method in vibrations*. New York: Macmillan Publishing Co. Inc, 1967.

[30] Barton, RA, Ilic, B, vander Zande, AM, et al. High, size-dependent quality factor in an array of graphene mechanical resonators. *Nano Lett* 2011; 11: 1232–1236.

[31] Adiga, VP, Ilic, B, Barton, RA, et al. Modal dependence of dissipation in silicon nitride drum resonators. *Appl Phys Lett* 2011; 99: 253103.

[32] Adiga, VP, Ilic, B, Barton, RA, et al. Approaching intrinsic performance in ultra-thin silicon nitride drum resonators. *J Appl Phys* 2012; 112: 064323.

[33] Murphy, KD, and Zhang, Y. Vibration and stability of a cracked translating beam. *J Sound Vib* 2000; 237: 319–335.

[34] Ouakad, HM, and Younis, MI. Natural frequencies and mode shapes of initially curved carbon nanotube resonators under electric excitation. *J Sound Vib* 2011; 330: 3182–3195.

[35] Dorfmann, L, and Ogden, RW. Nonlinear electroelasticity: material properties, continuum theory and applications. *Proc R Soc A Math Phys Eng Sci* 2017; 473: 20170311.

[36] Xie, YX, Liu, JC, and Fu, YB. Bifurcation of a dielectric elastomer balloon under pressurized inflation and electric actuation. *Int J Solids Struct* 2016; 78: 182–188.

[37] Pruchnicki, E. Homogenization of a second order plate model. *Math Mech Solids* 2017; 23: 1323–1332.

[38] Wang, F-F, Steigmann, DJ, and Dai, H-H. On a uniformly-valid asymptotic plate theory. *Int J Non-Lin Mech* 2019; 112: 117–125.

[39] Wang, F-F, Dai, H-H, and Giorgio, I. A numerical comparison of the uniformly valid asymptotic plate equations with 3D model: clamped rectangular incompressible elastic plates. *Math Mech Solids*. Epub ahead of print 5 July 2021. DOI: 10.1177/10812865211025583.

[40] Dai, H-H, and Song, Z-L. On a consistent finite-strain plate theory based on three-dimensional energy principle. *Proc R Soc A Math Phys Eng Sci* 2014; 470: 20140494.

[41] Boudaoud, A, Patricio, P, Couder, Y, et al. Dynamics of singularities in a constrained elastic plate. *Nature* 2000; 407: 718–720.

[42] McLachlan, NW. *Bessel functions for engineers*. 2nd ed. Oxford: Clarendon Press, 1955.

[43] Press, WH, Teukolsky, SA, Vetterling, WT, et al. *Numerical recipes in Fortran*. 2nd ed. Cambridge: Cambridge University Press, 1992.

[44] Krylov, S, Harari, I, and Cohen, Y. Stabilization of electrostatically actuated microstructures using parametric excitation. *J Micromech Microeng* 2005; 15: 1188–1204.

[45] Alsaleen, FM, Younis, MI, and Ouakad, HM. On the nonlinear resonances and dynamic pull-in of electrostatically actuated resonator. *J Micromech Microeng* 2009; 19: 045013.

[46] Davini, C, Favata, A, and Paroni, R. The Gaussian stiffness of graphene deduced from a continuum model based on molecular dynamics potentials. *J Mech Phys Solids* 2017; 104: 96–114.

[47] Lindahl, N, Midtvedt, D, Svensson, J, et al. Determination of the bending rigidity of graphene via electrostatic actuation of buckled membranes. *Nano Lett* 2012; 12: 3526–3531.

[48] Sheplak, M, and Dugundji, J. Large deflections of clamped circular plates under initial tension and transitions to membrane behavior. *J Appl Mech* 1998; 65: 107–115.

[49] Saghir, S, Bellaredj, M, Ramini, A, et al. Initially curved microplates under electrostatic actuation: theory and experiment. *J Micromech Microeng* 2016; 26: 095004.

Appendix I

When there is no electrostatic loading ($\alpha_4 = 0$), the linear parts of equations (16) and (17) are the following:

$$\frac{\partial^2 W_1}{\partial \tau^2} - \alpha_1 \left(\frac{1}{\xi} \frac{\partial W_1}{\partial \xi} + \frac{\partial^2 W_1}{\partial \xi^2} \right) = 0, \tag{28}$$

$$\frac{\partial^2 U_1}{\partial \tau^2} - \alpha_5 \left(\frac{\partial^2 U_1}{\partial \xi^2} + \frac{1}{\xi} \frac{\partial U_1}{\partial \xi} - \frac{U_1}{\xi^2} \right) = 0. \tag{29}$$

The two displacements are assumed to have the following forms:

$$W_1(\xi, \tau) = \phi(\xi) e^{i\omega \tau}, \quad U_1(\xi, \tau) = \psi(\xi) e^{i\varpi \tau}, \tag{30}$$

Table 1. The values of the first ten η_is and β_is [42].

i	1	2	3	4	5	6	7	8	9	10
η_i	2.4048	5.5201	8.6537	11.7915	14.9309	18.0711	21.2116	24.3525	27.4935	30.6346
β_i	3.8317	7.0156	10.1735	13.3237	16.4706	19.6159	22.7601	25.9037	29.0468	32.1897

here ω and ϖ are the (dimensionless) eigenfrequencies of the out-of-plane and in-plane displacements, respectively. Substituting equation (28) into equations (26) and (27), we have:

$$\frac{d^2\phi}{d\xi^2} + \frac{1}{\xi}\frac{d\phi}{d\xi} + \eta^2\phi = 0, \tag{31}$$

$$\frac{d^2\psi}{d\xi^2} + \frac{1}{\xi}\frac{d\psi}{d\xi} + \left(\beta^2 - \frac{1}{\xi^2}\right)\psi = 0, \tag{32}$$

here η and β are defined as the following:

$$\eta = \frac{\omega}{\sqrt{\alpha_1}}, \quad \beta = \frac{\varpi}{\sqrt{\alpha_5}}. \tag{33}$$

Equations (29) and (30) are the Bessel equations of order 0 and 1, respectively. Their solutions are the following [42]:

$$\phi(\xi) = AJ_o(\eta\xi) + BY_o(\eta\xi), \quad \psi(\xi) = CJ_1(\beta\xi) + DY_1(\beta\xi), \tag{34}$$

here J_o and Y_o are the first and second kinds of the Bessel functions of order 0, respectively; J_1 and Y_1 are the first and second kinds of the Bessel functions of order 1, respectively. Because $Y_o(\infty) = \infty$ and $Y_1(\infty) = \infty$, $B = D = 0$ must be taken in order to have finite displacements. Equation (32) now becomes the following:

$$\phi(\xi) = \sum_{i=1}^{\infty} A_i J_o(\eta_i\xi), \quad \psi(\xi) = \sum_{i=1}^{\infty} C_i J_1(\beta_i\xi). \tag{35}$$

It is not hard to verify that with the solution forms of equation (33), the boundary conditions of equation (7) are automatically satisfied due to our axisymmetric assumptions on the membrane deformations. Here, η_i is the ith zero point of $J_o(\eta_i) = 0$ and β_i is the ith zero point of $J_1(\beta_i) = 0$. The values of the first ten η_is and β_is are given in Table 1 [42].

From equation (31), we can have a comparison on the eigenfrequencies of U_1 and W_1, which yields the following equation in conjunction with equation (11):

$$\frac{\varpi_i}{\omega_j} = \sqrt{\frac{\alpha_5}{\alpha_1}}\frac{\beta_i}{\eta_j} = \sqrt{\frac{1}{(1+\nu)\epsilon_o}}\frac{\beta_i}{\eta_j}. \tag{36}$$

For graphene, $\nu = 0.165$ and the initial strain is set as a very large value of $\epsilon_o = 1\%$. From equation (34) and Table 1, we have $\varpi_1/\omega_{10} = 1.15588$ by taking $i = 1$ and $j = 10$. Physically this means that the first eigenfrequency of the in-plane displacement (ϖ_1) is larger than the tenth of the out-of-plane displacement (ω_{10}). Furthermore, $\epsilon_o = 1\%$ is extremely large strain and a smaller ϵ_o leads to a larger ratio of ω_1/ϖ_{10} as seen in equation (34). In a real application, the excitation frequency is much smaller than the first in-plane eigenfrequency of ϖ_1. Mainly, a few transverse modes (less than 10) are excited and the in-plane modes are hardly excited. This is the physical mechanism to de-couple the in-plane and out-of-plane vibrations.